Supporting Information

for

Identifying high-mobility tetracene derivatives using a non-adiabatic molecular dynamics approach

Orestis George Ziogos[a], Samuele Giannini[a], Matthew Ellis[a], and Jochen Blumberger[a]

[a]Department of Physics and Astronomy and Thomas Young Centre, University College London, Gower Street, London WC1E 6BT, UK.

Contents

Description of the FOB-SH methodology

Outline of FOB-SH

The fragment orbital-based surface hopping method (FOB-SH) is a semi-empirical approach designed to follow the time evolution of an excess charge carrier in extended condensed-phase systems in time. This approach allows the efficient and accurate calculation of the electronic Hamiltonian and nuclear derivatives (forces, non-adiabatic coupling vectors) in systems with thousands of atoms. It relies on the assumptions that the full many-body electronic wavefunction can be replaced by a one-particle wavefunction $\Psi(t)$ for the excess charge carrier, and that the latter can be expressed in a quasi-diabatic basis made up of orthogonalized frontier molecular orbitals (FMOs) (see Eq. 1 in the main text). This set of $\{\phi_l\}$ orbitals is obtained by means of Löwdin transformations of the non-orthogonal FMOs $\{\varphi_m\}$ of single molecules according to

$$\phi_l = \sum_{m=1}^{M} T_{ml}\varphi_m \, , \tag{1}$$

in which $T_{ml} = \left[\mathbf{S}^{-1/2}\right]_{ml}$, with $\mathbf{S}$ being the overlap matrix of the fragment orbital basis set $S_{ml} = \langle \varphi_m | \varphi_l \rangle$. The localized FMOs $\{\varphi_m\}$ are obtained from explicit Density Functional Theory (DFT) calculations during the parametrization stage (further computational details and procedural information are reported further below in subsection *Analytic overlap method: computational details*).

A key feature of FOB-SH is that explicit electronic structure calculation of the Hamiltonian is avoided during time propagation, since the latter is instead reconstructed using a tight-binding approach based on parametrizations of electronic couplings and site energies. This strategy allows the simulation of large systems (thousands of atoms) over long time scales (in the order of picoseconds). The description of the diagonal elements of the Hamiltonian (site energies) relies on classical force fields (FF) and is given in more detail in subsection *Classical reorganization energy fitting method*. On the other hand, the electronic couplings or charge transfer integrals (CTI) are computed using the efficient analytic overlap method (AOM) [Gajdos2014] (see subsection *Analytic overlap method: computational details*).

Besides the electronic Hamiltonian matrix elements, the time-dependent Schrödinger equation (Eq. 2 in the main text) requires the determination of the non-adiabatic coupling elements (NACEs) $d_{kl} = \langle \phi_k | \dot{\phi}_l \rangle$ which in our quasi-diabatic basis set are smooth functions and always close to zero by definition. Nevertheless, d_{kl} can be calculated at each time step using the relation with the non-orthogonal NACEs $\left(d'_{kl} = \left[\mathbf{D}'\right]_{kl} = \langle \varphi_k | \dot{\varphi}_l \rangle\right)$,

$$d_{kl} = \left[\mathbf{T}^\dagger \mathbf{D}' \mathbf{T}\right]_{kl} + \left[\mathbf{T}^\dagger \mathbf{S} \dot{\mathbf{T}}\right]_{kl} \tag{2}$$

Both $\mathbf{D}'_{kl}$ and $\dot{\mathbf{T}}$ are obtained via a finite difference scheme between t and $t + \Delta t$.

As mentioned in the main text, in surface hopping molecular dynamics, the nuclear degrees of freedom are propagated on a single adiabatic potential energy surface $E_i \equiv \left[\mathbf{H}^{\text{ad}}\right]_{ii}$, which is obtained

by a unitary transformation of the diabatic Hamiltonian $\mathbf{H}$ (eq. 3), where $\mathbf{U}$ is the transformation matrix. The corresponding adiabatic states are denoted by $\{\psi_i\}$.

$$\mathbf{H}^{\text{ad}} = \mathbf{U}^\dagger \mathbf{H} \mathbf{U} \tag{3}$$

$$\psi_i = \sum_{k=1}^{M} U_{ki} \phi_k \tag{4}$$

The nuclear forces on the adiabatic state i, $\vec{F}_{I,i}$, can be obtained from the gradients of the Hamiltonian matrix elements in the diabatic representation using the Hellmann-Feynman theorem,

$$\vec{F}_{I,i} = -\nabla_I E_i = -\nabla_I \langle \psi_i | H | \psi_i \rangle = -\left[\mathbf{U}^\dagger \left(\nabla_I \mathbf{H} \right) \mathbf{U} \right]_{ii}, \tag{5}$$

where $\left[\nabla_I \mathbf{H} \right]_{kl} \equiv \nabla_I H_{kl} = \nabla_I \langle \phi_k | H | \phi_l \rangle$. The last identity in Eq. 5 has been shown explicitly by Spencer et al. [Spencer2016]. In practice, the gradients of the diagonal and off-diagonal elements are obtained by using forces that come from the classical FF and finite difference of the orbital overlap according to the AOM. The probability to hop from the current (active) adiabatic state i to another state j in Tully's fewest switch algorithm is given by

$$g_{ij} = \max \left[0, \frac{-2\,\text{Re}\left(a_{ij}^* d_{ij}^{\text{ad}} \right)}{a_{ii}} \Delta t \right], \tag{6}$$

where $a_{ij} = c_i^* c_j$ is the electronic density matrix, c_i being the expansion coefficients of the wavefunction in the adiabatic basis, $\Psi(t) = \sum_{i=1}^{M} c_i(t) \psi_i \left(\vec{R}(t) \right)$, $d_{ja}^{\text{ad}} = \langle \psi_j | \dot{\psi}_a \rangle$ are the adiabatic NACEs, which are calculated from the diabatic NACEs $\left(d_{kl} \equiv \left[\mathbf{D} \right]_{kl} \right)$:

$$d_{ja}^{\text{ad}} = \left[\mathbf{U}^\dagger \mathbf{D} \mathbf{U} \right]_{ja} + \left[\mathbf{U} \dot{\mathbf{U}} \right]_{ja}, \tag{7}$$

Algorithmic details

There are certain crucial requirements that surface hopping dynamics should fulfill in order to give accurate and unbiased charge propagation, such as energy conservation and detailed balance (adiabatic states populated according to Boltzmann statistic), internal consistency between electron and nuclear populations, and trivial crossing detection during the dynamics in order to avoid unphysical spurious long-range charge transfers. FOB-SH has been tailored to achieve all these criteria, thus giving a correct charge carrier dynamics [Carof2017, Giannini2018].

In particular, energy conservation and detailed balance in FOB-SH are obtained by adjusting the nuclear velocity component in the direction of the non-adiabatic coupling vectors (NACVs)

$\vec{d}_{I,an}^{\,\text{ad}} = \langle \psi_a | \nabla_I \psi_n \rangle$, as previously prescribed by Tully [Tully1990], whenever a surface hop has enough kinetic energy to compensate the transition in potential energy. An exact expression for the NACVs in terms of available nuclear gradients in the diabatic basis has been derived by Carof et al. within FOB-SH framework [Carof2017]. This adjustment ensures that:

$$E_{\text{tot}}(\vec{R}) = T_a(\vec{R}) + E_a(\vec{R}) = T_n(\vec{R}) + E_n(\vec{R}), \tag{8}$$

where E_a and E_n correspond to the potential energy and T_a and T_n to the nuclear kinetic energy before and after the hop. If a surface hop does not have enough energy to fulfill Eq.8, it is rejected and velocities are reversed.

Internal inconsistency between electronic and nuclear dynamics is a well-known problem in surface hopping, mainly caused by the lack of decoherence of the nuclear wavepacket when leaving the crossing region. In FOB-SH the decoherence correction is reintroduced using the algorithm proposed by Granucci and Persico [Granucci2007], where all non-active adiabatic populations c_i are damped at each time step by $c_i \rightarrow c_i \exp(-\Delta t / \tau_{ia})$ while the active state population is scaled to ensure norm conservation. τ_{ia} is the decoherence time taken equal to: $\tau_{ia} = \hbar / |E_i - E_a|$ [Giannini2018].

Biased dynamics due to the presence of trivial (or unavoided) crossing becomes a substantial limitation when performing charge transport simulations with surface hopping. A trivial crossing event occurs when two energy surfaces cross with zero couplings between them leading to an actual reordering of the state indices. Physically, such crossings occur when the adiabatic states are not interacting, i.e. when the adiabatic wavefunctions are localized at distant regions in space. Since surface hopping uses a finite molecular dynamics time step, the change in the state ordering within one step might go undetected giving rise to serious issues such as continuation of the nuclear dynamics on an incorrect active state, discontinuity in the nuclear forces that affect the energy conservation, erroneous calculation of time derivatives, especially d_{ji}^{ad}, deteriorating excited state population and detailed balance, and – most seriously in the context of charge transport – spurious and unphysical long-range charge transfer events between spatially distant states of similar energy.

We have recently tackled these problems within the FOB-SH framework using a state tracking algorithm for the correct assignment of the states indices during time propagation [Giannini2018] and adopting the self-consistent surface hopping approach (SC-FSSH) of Wang and Prezhdo [Wang2014a] to improve the hopping probability of Eq. 6 near the crossing point.

Lastly, a further source of inaccuracy is due to the so-called decoherence-induced spurious charge transfer events (DCICTs) resulting to unphysical charge displacements. In fact, after an unfavored surface hop (i.e. hop with a small hopping probability in Eq. 6) between adiabatic states localized in different regions in space, the decoherence correction will move the electronic wavefunction $\Psi(t)$ closer to the new active state $\psi_a(t)$, thus leading, in some cases, to unphysical charge transfer. We have proposed a simple correction scheme to this problem, defining a moving and flexible active region containing virtually all of the charge carrier density within which the decoherence is still active [Giannini2018]. However, charge transfers outside this active region are not allowed, thus avoiding spurious long-range transfers. This enhanced FOB-SH algorithm has been used in all the simulations done in this work.

Systems under study

Table S-1 A listing of all systems under study with details regarding the supercell dimensions, the columnar direction that facilitates charge transfer, and both the number of total and QM active molecules. The last column contains the root mean squared displacement (RMSD) at 300K, calculated from equilibrated MD trajectories at the microcanonical statistical ensemble. A decomposition of the total RMSD to core and side chain contributions is carried out for systems with side chains longer than methyl groups

System	CCDC Deposition Number / Database Identifier	Triclinic supercell parameters a, b, c (Å); α, β, γ (°)	Columnar direction	Number of total / QM active molecules	RMSD (Å)
Tetracene (TETCEN)	1269538/ TETCEN	197.50, 150.75, 27.06; 100.30, 113.20, 86.30	N/A	2500/49	0.53±0.02
1,4,7,10-Tetramethyltetracene (TMT)	723050/ GUMZIY	626.11, 26.77, 34.70; 83.82, 89.80, 88.04	a	1500/300	0.56±0.06
1,4,7,10-Tetraethyltetracene (TET)	723051/ GUMZOE	239.95, 28.47, 38.94; 69.22, 87.00, 78.94	a	540/60	0.42±0.03[*] 0.38±0.03[†] 0.47±0.03[§]
1,4,7,10-Tetrapropyltetracene (TPrT)	723052/ GUMZUK	632.25, 18.58, 25.60; 103.76, 90.45, 104.02	a	500/125	0.74±0.09[*] 0.71±0.09[†] 0.76±0.08[§]
1,4,7,10-tetrakis(n-Butyl)tetracene (TBuT)	642337/ HIGNIV	33.27, 592.37, 21.54; 90.00, 127.46, 90.00	b	500/125	0.67±0.07[*] 0.64±0.07[†] 0.69±0.06[§]
1,4,7,10-Tetrapentyltetracene (TPeT)	723053/ GUNBAT	643.25, 22.56, 27.10; 85.63, 84.72, 81.70	a	500/125	0.74±0.09[*] 0.69±0.09[†] 0.78±0.08[§]
1,4,7,10-Tetrahexyltetracene (THT)	723054/ GUNBEX	33.04, 591.87, 26.41; 90.00, 123.57, 90.00	b	500/125	0.86±0.08[*] 0.82±0.09[†] 0.86±0.08[§]
1,4,7,10-Tetraisobutyltetracene (TiBuT)	746563/ DUWHEJ	658.37, 22.30, 23.86; 85.41, 84.29, 84.95	a	500/125	0.85±0.09[*] 0.79±0.10[†] 0.93±0.08[§]
1,4,7,10-Tetraisopropyltetracene (TiPeT)	746565/ DUWHOT	601.12, 30.30, 21.95; 90.00, 106.37, 90.00	a	500/125	0.86±0.06[*] 0.78±0.06[†] 0.90±0.06[§]
1,4-Dipropyltetracene (DPrT)	761527/ DUWPER	35.38, 553.80, 35.74; 90.00, 103.22, 90.00	b	1600/400	0.45±0.02[*] 0.42±0.02[†] 0.46±0.02[§]

[*]: Total RMSD

[†]: tetracene core RMSD

[§]: side chain RMSD.

Utilized force field and molecular dynamics simulations details

The classical force field (FF) utilized for molecular dynamics (MD) simulations of alkylated tetracenes consists of constant topology bonded terms, with harmonic interactions for bond stretching and bending and appropriate dihedral angle terms for torsions, and non-bonded terms in the form of the Lennard-Jones (LJ) potential for the quantification of dispersion interactions. The potential energy is given by the following expression:

$$E = \sum_{\text{bonds}} k_b (r - r_0)^2 + \sum_{\text{angles}} k_a (\theta - \theta_0)^2 + \sum_{\text{dihedrals}} \sum_{i=1}^{m_d} k_{d,i} \left[1 - \cos(n_{d,i}\phi - d_{d,i}) \right] +$$
$$+ \frac{1}{2} \sum_{i \neq j} 4\varepsilon_{ij} \left[\left(\frac{\sigma_{ij}}{r_{ij}} \right)^{12} - \left(\frac{\sigma_{ij}}{r_{ij}} \right)^6 \right] \tag{9}$$

Aliphatic carbon atoms are treated at the united atom level of description. The parameterization of the FF is based on a combination of the Generalized Amber Force Field (GAFF) and the Optimized Potential for Liquid Simulations (OPLS) FFs [Wang2004b, Jorgensen1984, Jorgensen1990]. The proper dihedral angle term dictating the torsional rotation about the aromatic-aliphatic carbon bond is adapted from the work of Marcon et al. [Marcon2008]. The suitability of the utilized FF was been demonstrated in the literature for a series of functionalized polyaromatic hydrocarbons in the condensed phase [Marcon2008, Cinacchi2004, Andrienko2006, Ziogos2015, Ziogos2018]. A depiction of the FF characteristics and the aforementioned proper dihedral angle are shown in Fig. S-1.
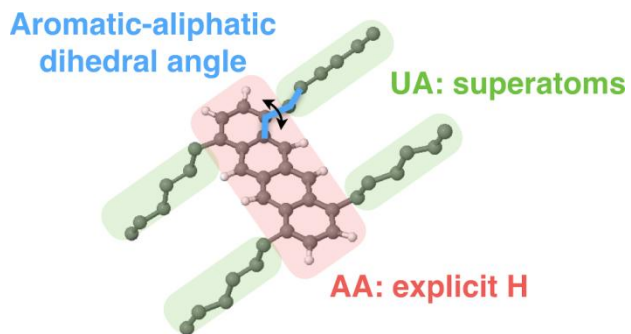

Fig. S-1 The decomposition to all-atom (AA) and united-atom (UA) levels of description for an alkylated tetracene. The aromatic-aliphatic dihedral angle is also highlighted.

As regards the aromatic-aliphatic carbon atom torsion term, the energetic minimum according to the term by Marcon et al. [Marcon2008] is situated at the ±90° state. This is in accordance with the experimental structure of TBuT, THT, and TiBuT molecular crystals (see Table S-1 for abbreviations). For the rest of the examined systems, this proper dihedral angle adopts a coplanar *cis/trans* conformation, thus rendering the utilization of the FF term by Marcon et al. inappropriate. In order to alleviate this issue, a dihedral energy term in the form of

$$E_{cis} = k_{cis} \left[1 - \cos(2\phi - 180) \right] \tag{10}$$

is utilized in order to impose the correct coplanar conformation. If this term is not taken into consideration, the coplanar conformation is the least favorable, since steric effects impose a double peak around the *cis* and *trans* conformations in the dihedral angle distribution profile. The

determination of the force constant k_{cis} is based on equilibrium MD simulations at the canonical statistical ensemble (NVT) at room temperature, aiming at the merging of the double peaks to a unique coplanar state. Simulation results for the dihedral angle under question are shown in Fig. S-2 for the TET molecular crystal. The value of 1.0 kcal/mol is adopted for all simulations of systems with coplanar side chain configurations.
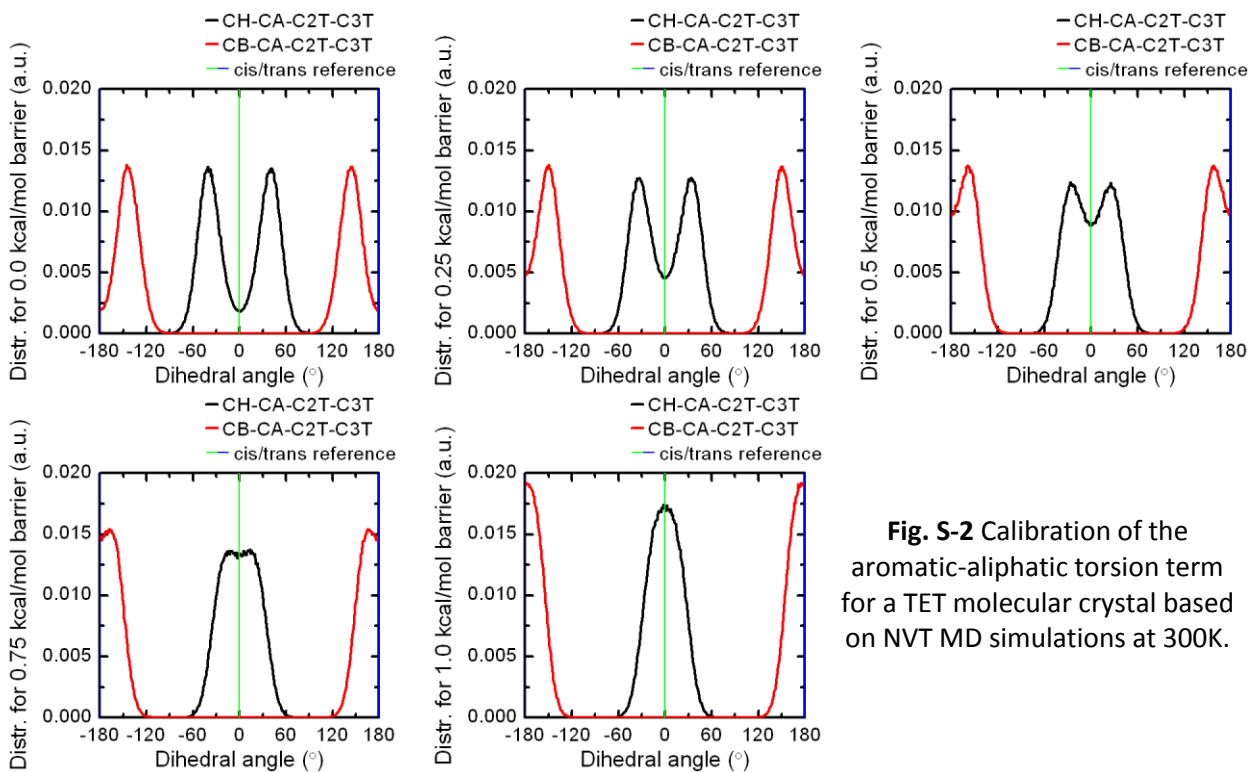

Fig. S-2 Calibration of the aromatic-aliphatic torsion term for a TET molecular crystal based on NVT MD simulations at 300K.

For the equilibration of all systems under study, MD simulations with typical periodic boundary conditions are carried out at the NVT statistical ensemble at a temperature of 300 K. A cutoff radius of 10 Å is adopted for LJ interactions. Atoms belonging to the same molecule which are topologically separated by a bond (1-2 interactions), an angle (1-3), or a proper dihedral angle (1-4) are excluded from non-bonded LJ interaction calculations. The Martyna-Tobias-Klein [Martyna1994] equations of motion are utilized for temperature control during NVT simulations, with an integration time step of 1.0 fs and a thermostat time constant of 100.0 fs. FF parameters are listed in the work of Ziogos and Theodorou [Ziogos2015].

Reorganization energy and charge transfer integral calculations details

Single molecule reorganization energy calculations are carried out by means of the 4-point scheme, according to which the hole reorganization energy is expressed as

$$\lambda = E_{(+)}^0 - E_0^0 + E_0^{(+)} - E_{(+)}^{(+)} \tag{11}$$

with E_0^0 and $E_{(+)}^{(+)}$ referring to the ground-state energies of the neutral and cationic states, respectively; $E_0^{(+)}$ to the energy of the cationic state using the equilibrium geometry of the neutral molecule; and $E_0^{(+)}$ to the energy of the neutral state considering the equilibrium geometry of the cationic molecular state.

Reorganization energies are calculated via density functional theory (DFT) structural optimization and single point energy evaluations at the B3LYP/6-311g(d) level of theory [Becke1993, Lee1988] using the NWCHEM package.

Charge transfer integrals (CTI) at the dimeric level of description are calculated using the CPMD package, utilizing the PBE functional [Perdew1996a, Perdew1996b] with Trouiller-Martins normconserving pseudopotentials [Trouiller1991] and a planewave basis set cutoff of 80 Ry. All calculated CTI values are subsequently scaled by a factor of 1.348 in order to account for the systematic underestimation inherent to density functional theory CTI calculations [Kubas2014].

Analytic overlap method: computational details

The ultrafast character of CTI calculations using the analytic overlap method (AOM) rests on the linear scaling law between CTIs and overlap integrals. Following this method, time consuming CTI calculations are reduced to frontier molecular orbital (FMO) overlap integral evaluations. At a second level of approximation, the FMO under study – namely the HOMO for hole conduction – is described by means of a minimal Slater-type orbital (STO) basis set, thus enabling efficient, on-the-fly, analytical calculations.

The projection of selected FMOs onto the minimal STO basis set is carried out using the CPMD package. DFT calculations are employed in order to retrieve converged Kohn-Sham (KS) orbitals at the single molecule level of description using the PBE functional with Trouiller-Martins normconserving pseudopotentials and a planewave basis set cutoff of 80 Ry. The KS orbital corresponding to the highest occupied state is subsequently expressed as a linear combination of STOs with projection completeness above 0.9. The methodology is described in detail in the literature by Gajdos et al. [Gajdos2014].

The scaling constants correlating CTIs and overlap integral values for all systems under study are calculated as follows: MD simulations at room temperature at the canonical statistical ensemble are carried out for the equilibration of a given periodic molecular crystal. From the equilibrated trajectories, a series of dimer configurations are extracted (typically 45) in order to carry out CTI calculations at the isolated dimer level of description. Moreover, the overlap integral values of the FMOs expressed at the STO basis set are calculated for the same dimer configurations. Finally, once all calculations are completed, both CTI and overlap integral values are available and the scaling constant $\bar{C}$ is evaluated via linear least squares regression of the form $|H| = \bar{C} \times |\bar{S}|$, where $|H|$ and $|\bar{S}|$ are the CTI and overlap integral values, respectively.

Linear scaling constants for all systems under study are summarized in Table S-2. The validity of the linear regression approach can be deducted from the correlation shown in Fig. S-3. A generalized value can be obtained either via a global fitting procedure using all available data points or by the average value of the scaling constants listed in Table S-2; nevertheless, a unique scaling constant was used for every system.

Table S-2 AOM linear scaling constants for all systems under study

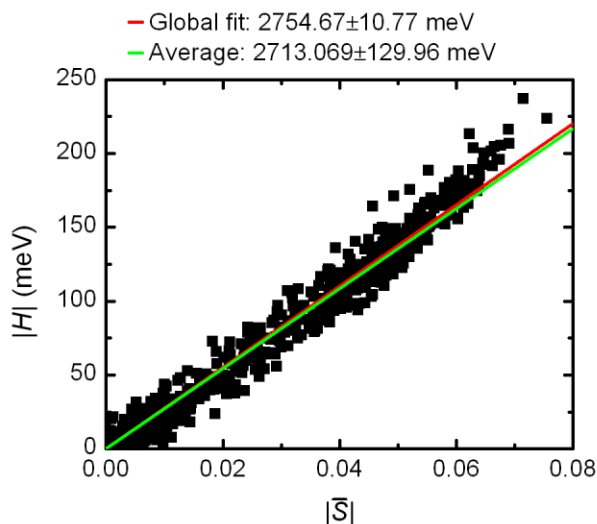| System	$\bar{C}$ (meV)	System	$\bar{C}$ (meV)
Tetracene	2538.70	TPeT	2620.37
TMT	2702.11	THT	2884.84
TET	2497.63	TiBuT	2744.33
TPrT	2735.61	TiPeT	2729.44
TBuT	2881.21	DPrT	2796.45

Fig. S-3 Correlation between FMO overlap integrals and CTIs for tetracene dimer configurations from all systems under study. The global fit refers to a least squares regression on all data; the average slope is calculated from Table S-2.

Classical reorganization energy fitting method

The intramolecular structural differences due to the transition from the neutral to the cationic state during charge transfer are taken into consideration as variations of the equilibrium bond lengths in the utilized classical force field. The applied procedure is the following:

- Carry out single molecule structural optimization by means of DFT calculations at the B3LYP/6-311g(d) level of theory for the neutral and charged molecule (using tight geometry optimization criteria in NWCHEM).
- Calculate the reorganization energy using the 4-point scheme.
- Identify significant bond length variations between the neutral and charged optimized structures.
- Assign appropriate atom types in order to account for the different bond lengths of the charged state.
- Alter in a systematic fashion the equilibrium bond lengths of the bond types associated with the structural variations of the charged molecule in order to match the classical and quantum reorganization energies. The equilibrium bond lengths are parametrically changed following the linear relationship $r_{k,0}^{\text{charged}} = r_{k,0}^{\text{neutral}} + \beta \Delta r_{k,\text{QM}}$, where $r_{k,0}^{\text{neutral}}$ the equilibrium length of bond type k at the neutral state according to the utilized classical force field, $\Delta r_{k,\text{QM}}$ the bond variation according to DFT structural optimization runs, and β the adjustable parameter.

The bond types associated with the structural reorganization of alkylated tetracenes in the cationic state are depicted in Fig. S-4. The differences in the aromatic carbon-carbon equilibrium bond length of 1.398 Å for all systems under study during FOB-SH simulations are listed in Table S-3.
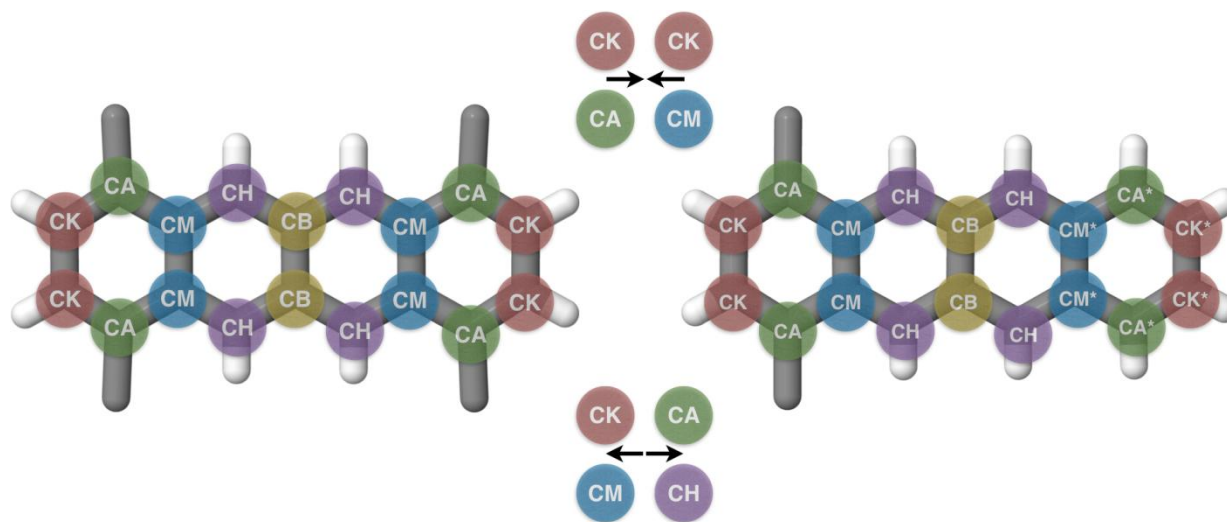

Fig. S-4 Atom types associated with the cationic state of tetra-substituted (left) and di-substituted (right) tetracene derivatives. Bond length expansion takes place for bond types CK-CA and CM-CH whereas contraction involves bond types CK-CK and CA-CM. In the case of di-substituted tetracene, bond length differentiations are not symmetric, hence the labeling CK*, CA*, and CM*.

Table S-3 Bond length differences (expressed in Å) between the neutral and cationic states of alkylated tetracenes with respect to the equilibrium FF value of 1.398 Å

	CK – CK	CK – CA	CA – CM	CM – CH
TETCEN	-0.01754	+0.01570	-0.01593	+0.01478
TMT	-0.01939	+0.01835	-0.01505	+0.01207
TET	-0.01948	+0.01859	-0.01586	+0.01195
TPrT	-0.01968	+0.01875	-0.01573	+0.01175
TBuT	-0.01985	+0.01886	-0.01574	+0.01163
TPeT	-0.01976	+0.01886	-0.01571	+0.01159
THT	-0.01974	+0.01887	-0.01571	+0.01158
TiBuT	-0.01944	+0.01847	-0.01561	+0.01175
TiPeT	-0.01951	+0.01817	-0.01546	+0.01199
DPrT	-0.02152	+0.02034	-0.01636	+0.01223
	CK* – CK*	CK* – CA*	CA* – CM*	CM* – CH
DPrT	-0.01578	+0.01380	-0.01461	+0.01406

Classical force field validation results

In order to assert the suitability of the utilized FF for the simulation of alkylated tetracene molecular crystals, a series of equilibrium structural properties were evaluated from room temperature MD simulations at the microcanonical statistical ensemble. These properties are the center of mass (CoM) radial distribution function and the angles formed by the normal and coplanar core vector with respect to the fixed Cartesian system of coordinates. The aromatic-aliphatic proper dihedral angle is also evaluated and compared with experimental data for all molecular crystals besides pristine tetracene and TMT. All structural validation results are presented throughout figures S-5 and S-13. Moreover, the root mean squared displacement (RMSD) for all systems under study is reported in Table S-1. The utilized FF exhibits a satisfactory agreement with available experimental data and relatively low RMSD values – especially for the tetracene cores.
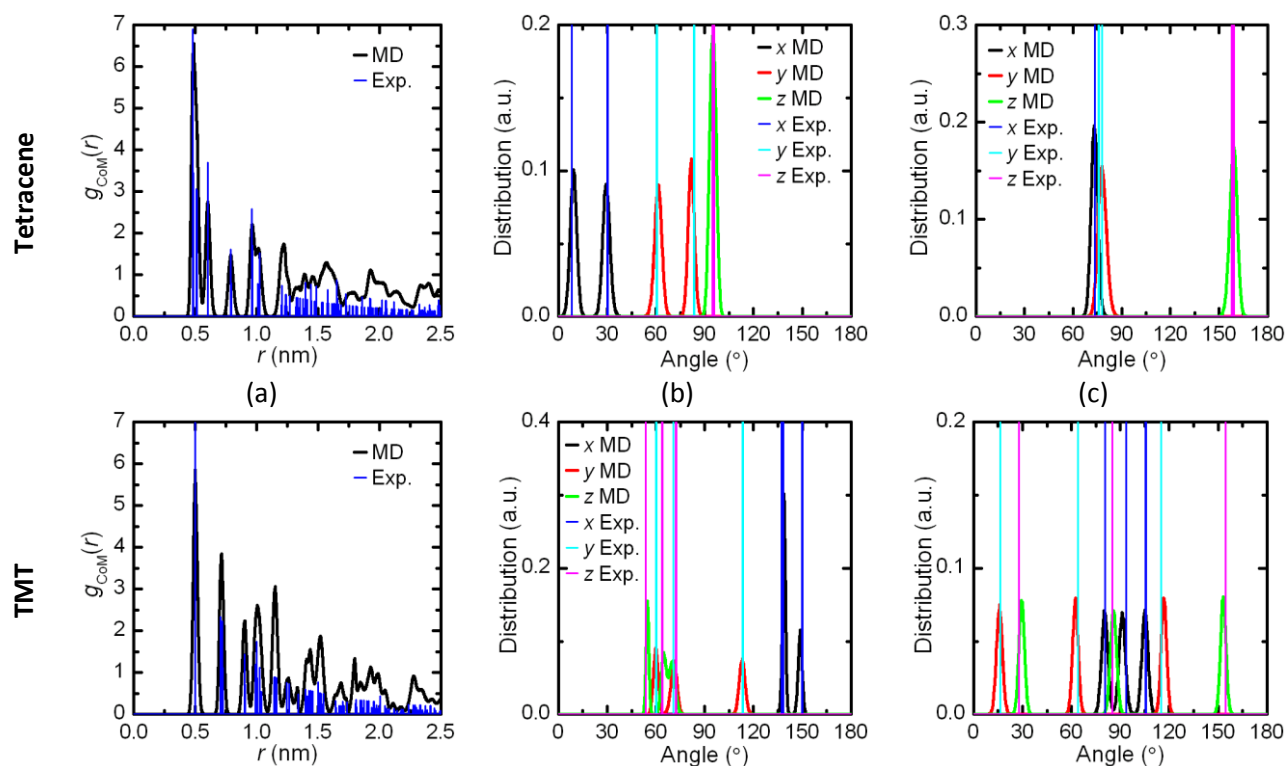
Fig. S-5 Structural validation of MD simulations at 300K of tetracene (top panel) and TMT (bottom panel) molecular crystals. (a) Center of mass (CoM) radial distribution function compared with experimental structure. The angles formed by the perpendicular and coplanar core vectors with respect to the fixed frame of coordinates are shown in (b) and (c), respectively, along with experimental reference values.
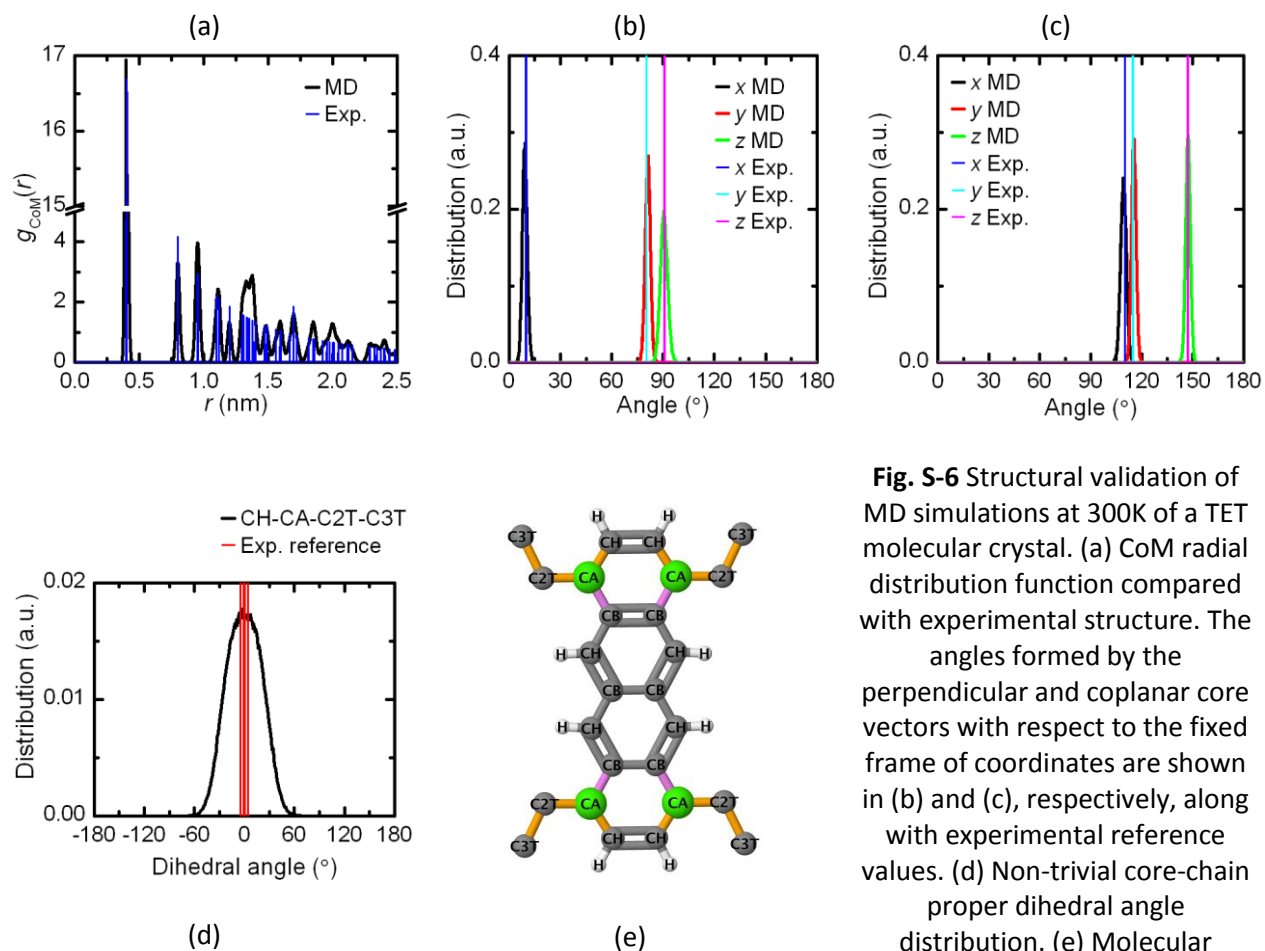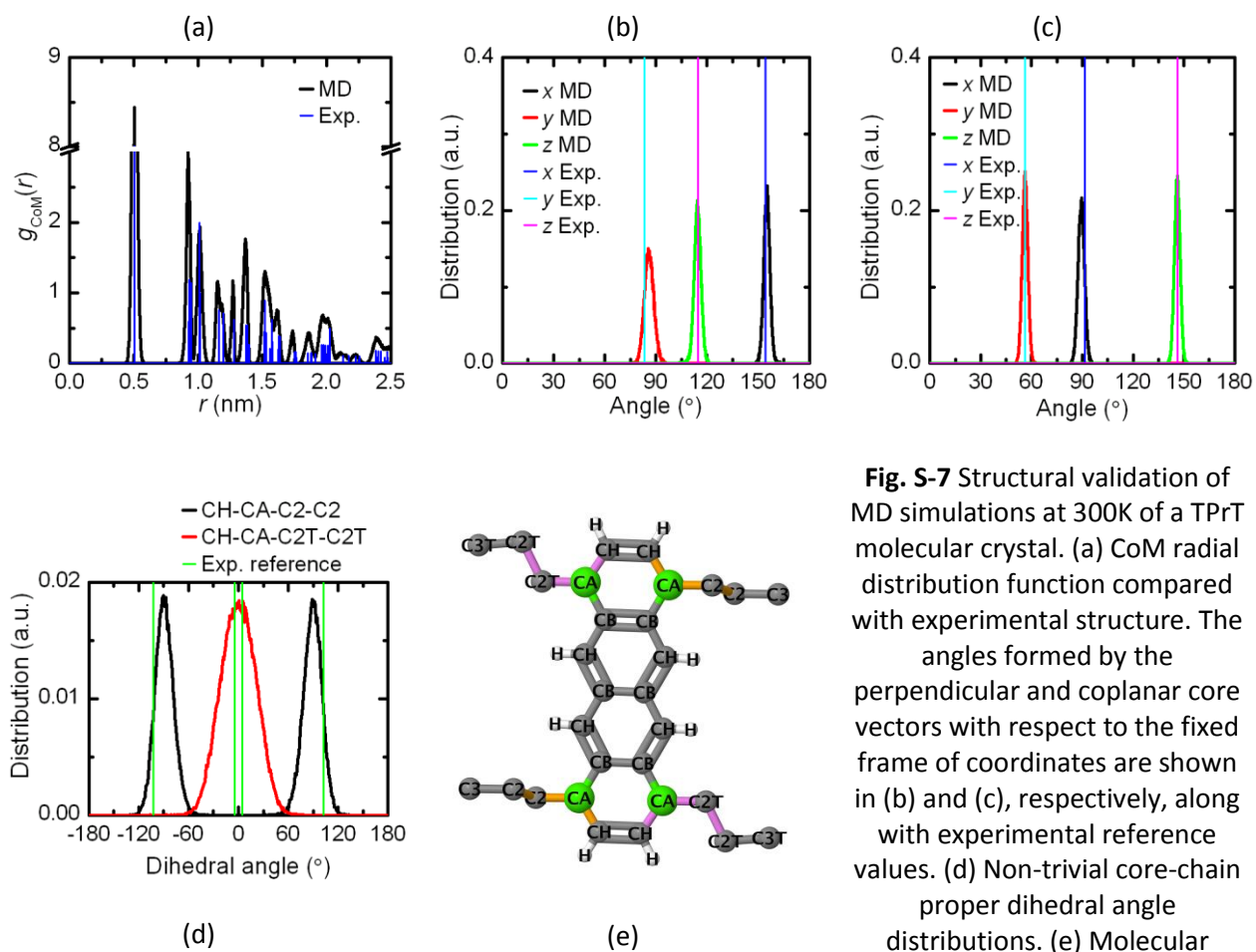
(a)

(b)

(c)

(d)

(e)

Fig. S-6 Structural validation of MD simulations at 300K of a TET molecular crystal. (a) CoM radial distribution function compared with experimental structure. The angles formed by the perpendicular and coplanar core vectors with respect to the fixed frame of coordinates are shown in (b) and (c), respectively, along with experimental reference values. (d) Non-trivial core-chain proper dihedral angle distribution. (e) Molecular structure.
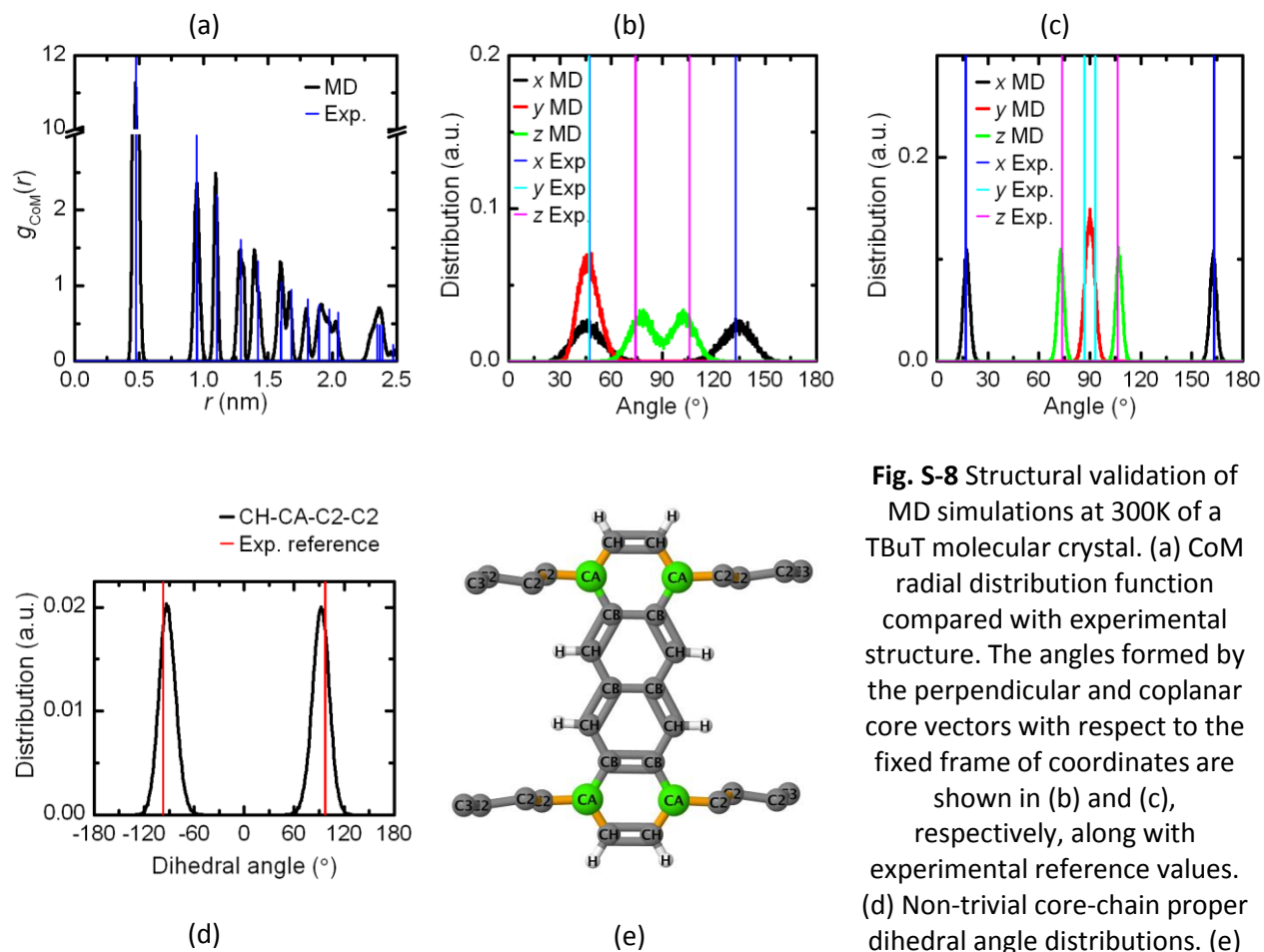
Fig. S-7 Structural validation of MD simulations at 300K of a TPrT molecular crystal. (a) CoM radial distribution function compared with experimental structure. The angles formed by the perpendicular and coplanar core vectors with respect to the fixed frame of coordinates are shown in (b) and (c), respectively, along with experimental reference values. (d) Non-trivial core-chain proper dihedral angle distributions. (e) Molecular structure.
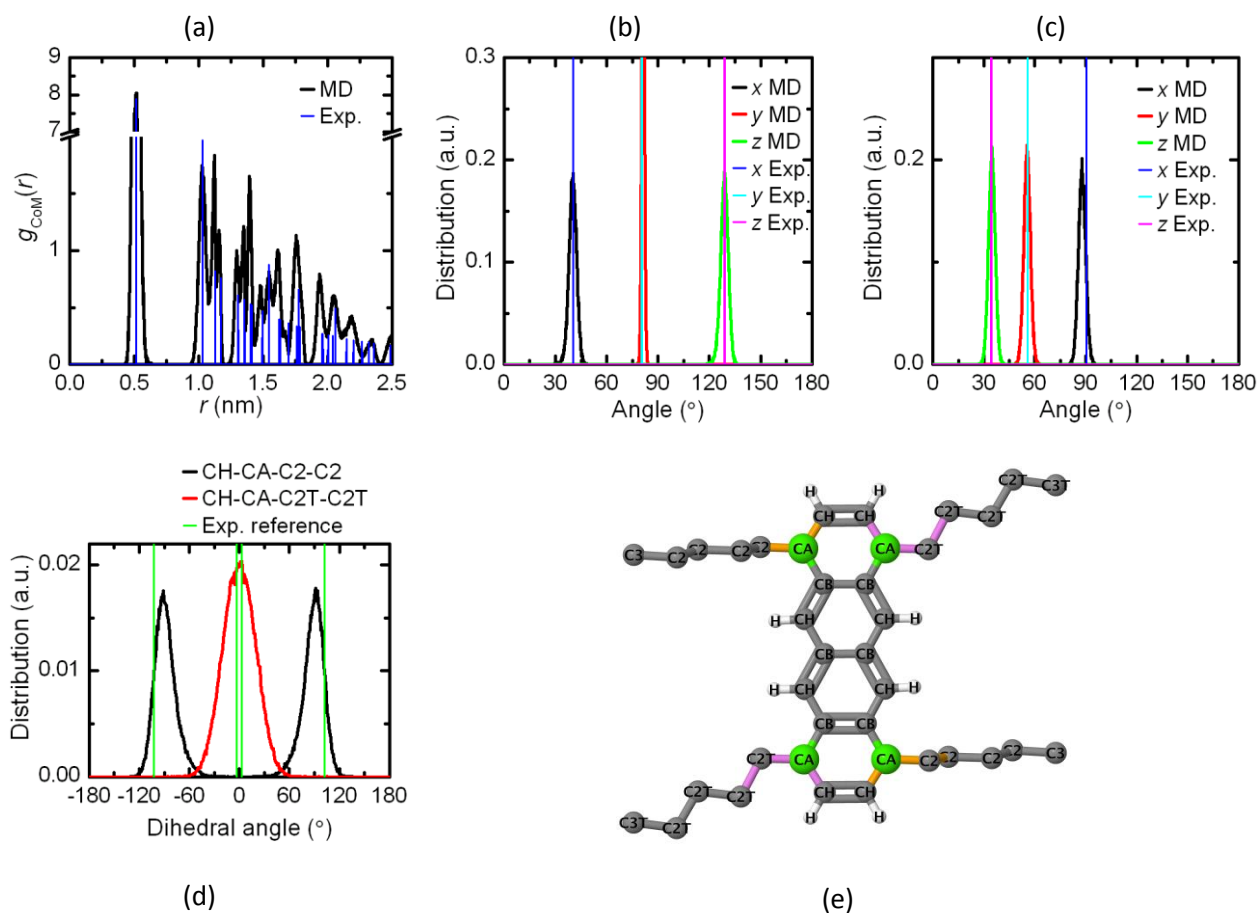
Fig. S-8 Structural validation of MD simulations at 300K of a TBuT molecular crystal. (a) CoM radial distribution function compared with experimental structure. The angles formed by the perpendicular and coplanar core vectors with respect to the fixed frame of coordinates are shown in (b) and (c), respectively, along with experimental reference values. (d) Non-trivial core-chain proper dihedral angle distributions. (e) Molecular structure.
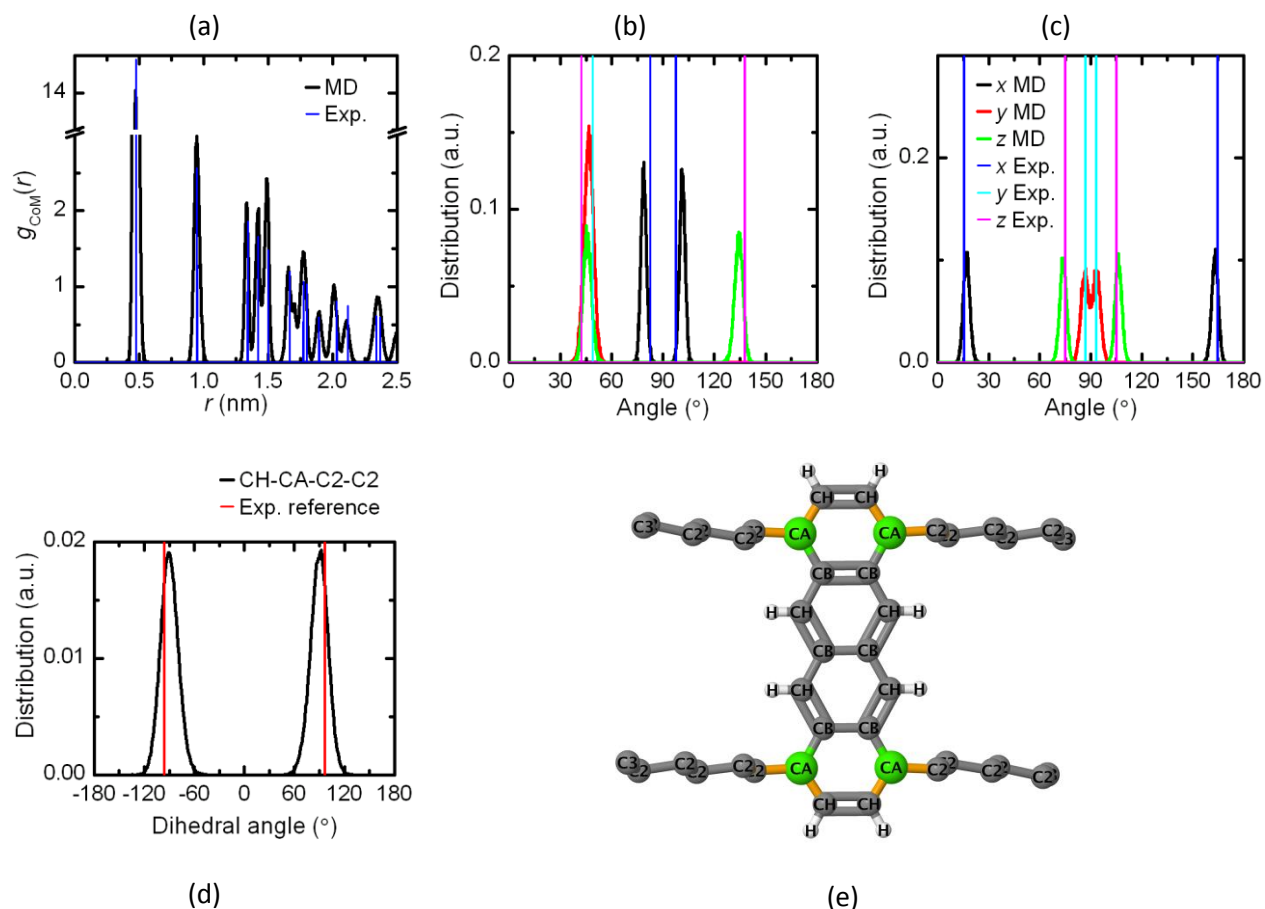
Fig. S-9 Structural validation of MD simulations at 300K of a TPeT molecular crystal. (a) CoM radial distribution function compared with experimental structure. The angles formed by the perpendicular and coplanar core vectors with respect to the fixed frame of coordinates are shown in (b) and (c), respectively, along with experimental reference values. (d) Non-trivial core-chain proper dihedral angle distributions. (e) Molecular structure.

Fig. S-10 Structural validation of MD simulations at 300K of a THT molecular crystal. (a) CoM radial distribution function compared with experimental structure. The angles formed by the perpendicular and coplanar core vectors with respect to the fixed frame of coordinates are shown in (b) and (c), respectively, along with experimental reference values. (d) Non-trivial core-chain proper dihedral angle distributions. (e) Molecular structure.
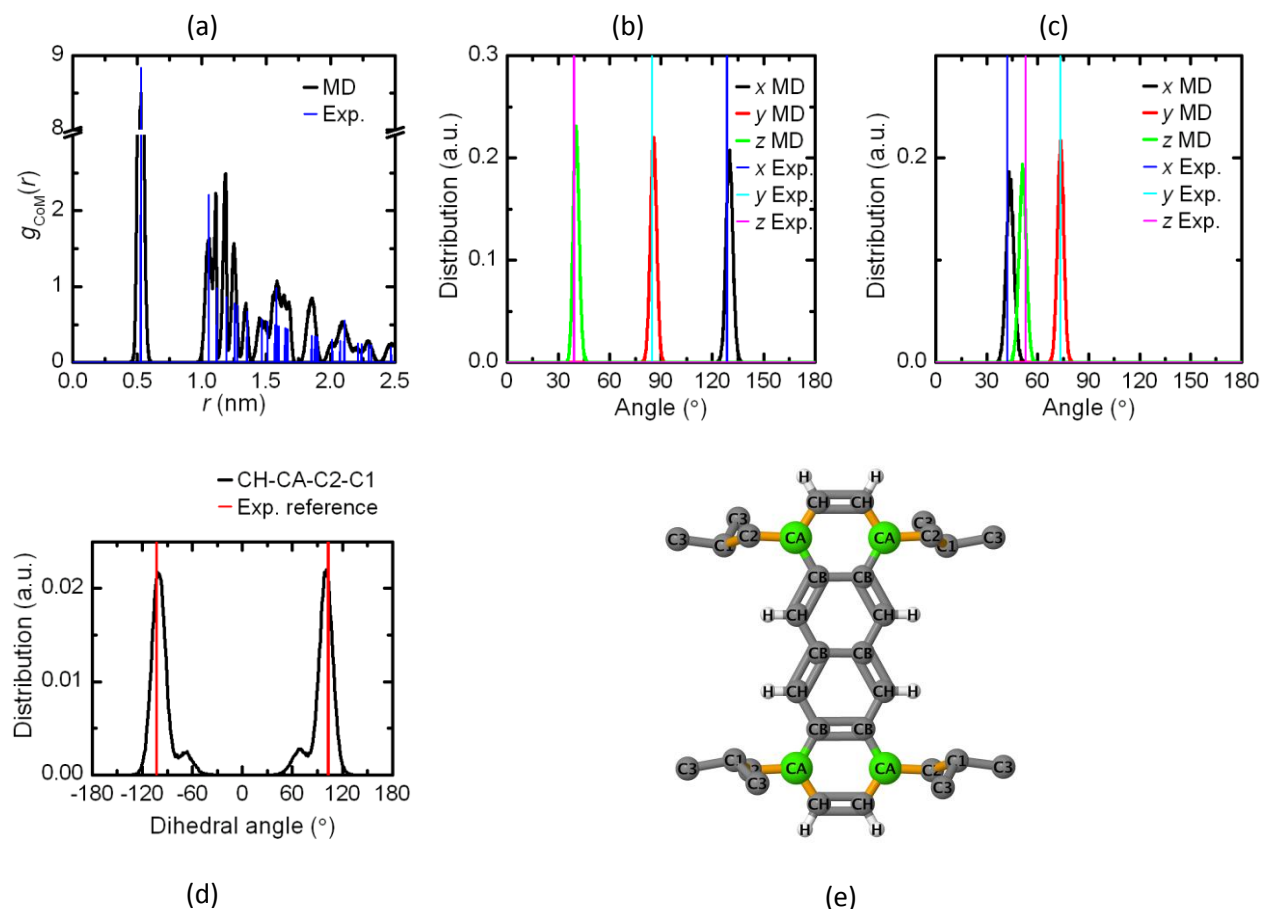
Fig. S-11 Structural validation of MD simulations at 300K of a TiBuT molecular crystal. (a) CoM radial distribution function compared with experimental structure. The angles formed by the perpendicular and coplanar core vectors with respect to the fixed frame of coordinates are shown in (b) and (c), respectively, along with experimental reference values. (d) Non-trivial core-chain proper dihedral angle distributions. (e) Molecular structure.
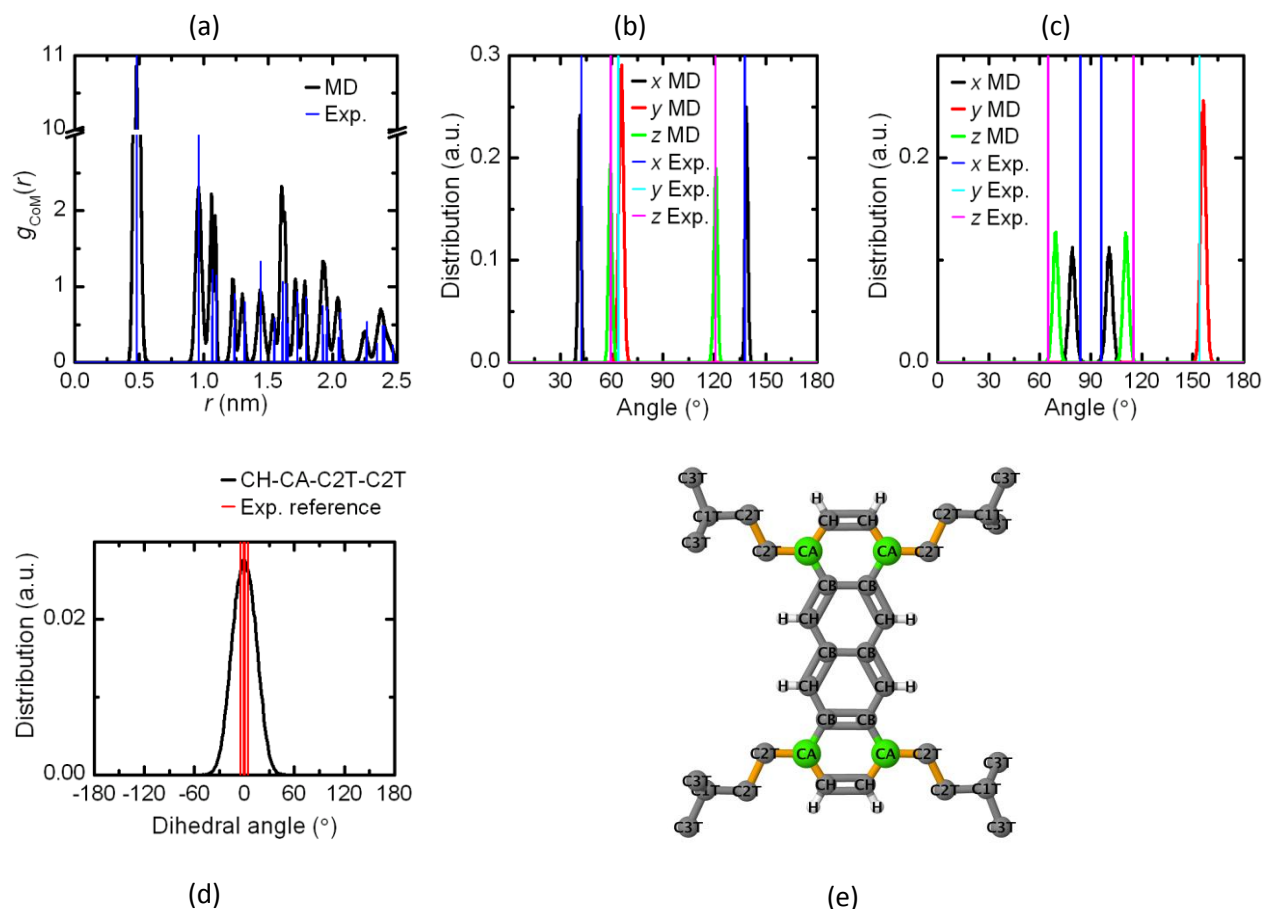
Fig. S-12 Structural validation of MD simulations at 300K of a TiPeT molecular crystal. (a) CoM radial distribution function compared with experimental structure. The angles formed by the perpendicular and coplanar core vectors with respect to the fixed frame of coordinates are shown in (b) and (c), respectively, along with experimental reference values. (d) Non-trivial core-chain proper dihedral angle distributions. (e) Molecular structure.
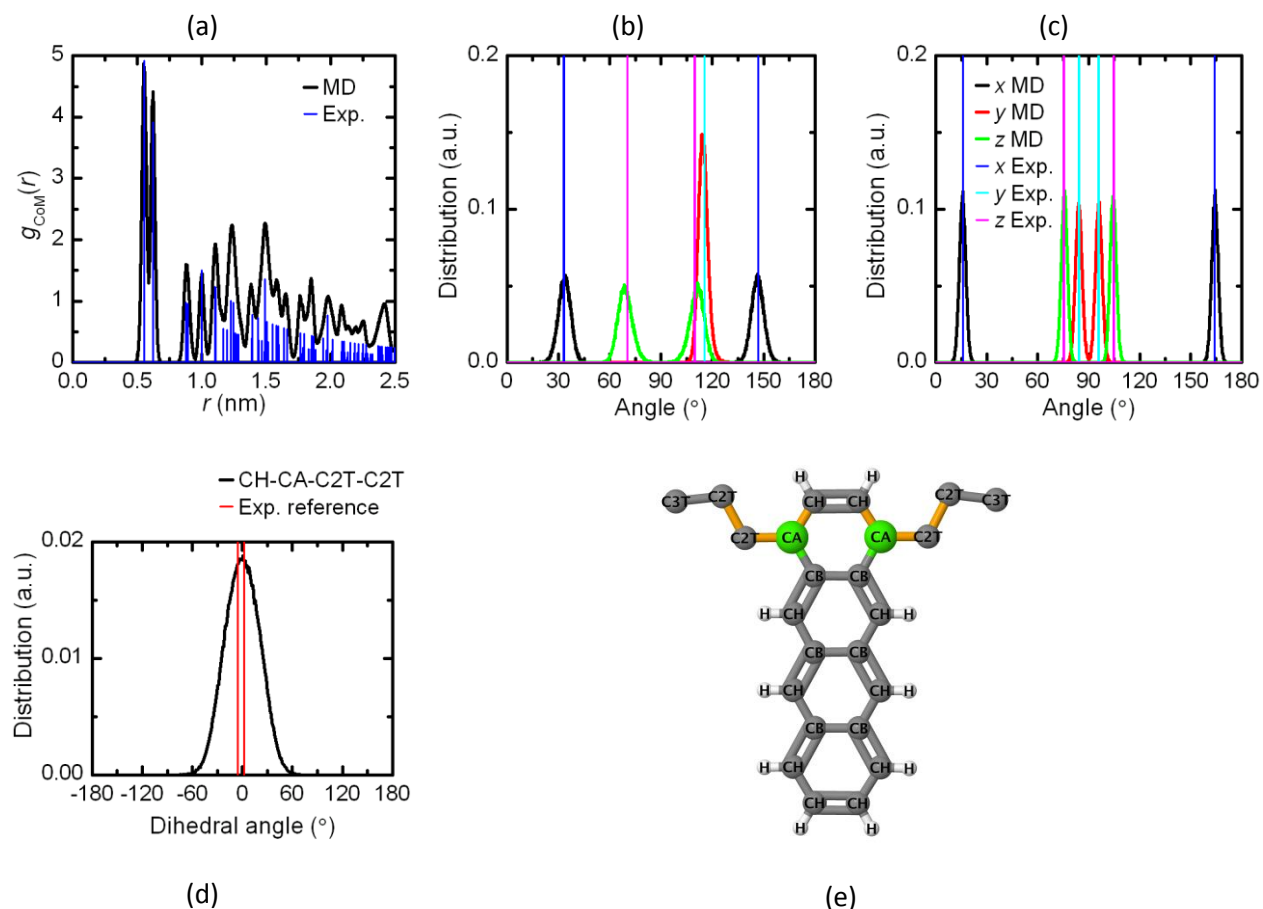
Fig. S-13 Structural validation of MD simulations at 300K of a DPrT molecular crystal. (a) CoM radial distribution function compared with experimental structure. The angles formed by the perpendicular and coplanar core vectors with respect to the fixed frame of coordinates are shown in (b) and (c), respectively, along with experimental reference values. (d) Non-trivial core-chain proper dihedral angle distributions. (e) Molecular structure.

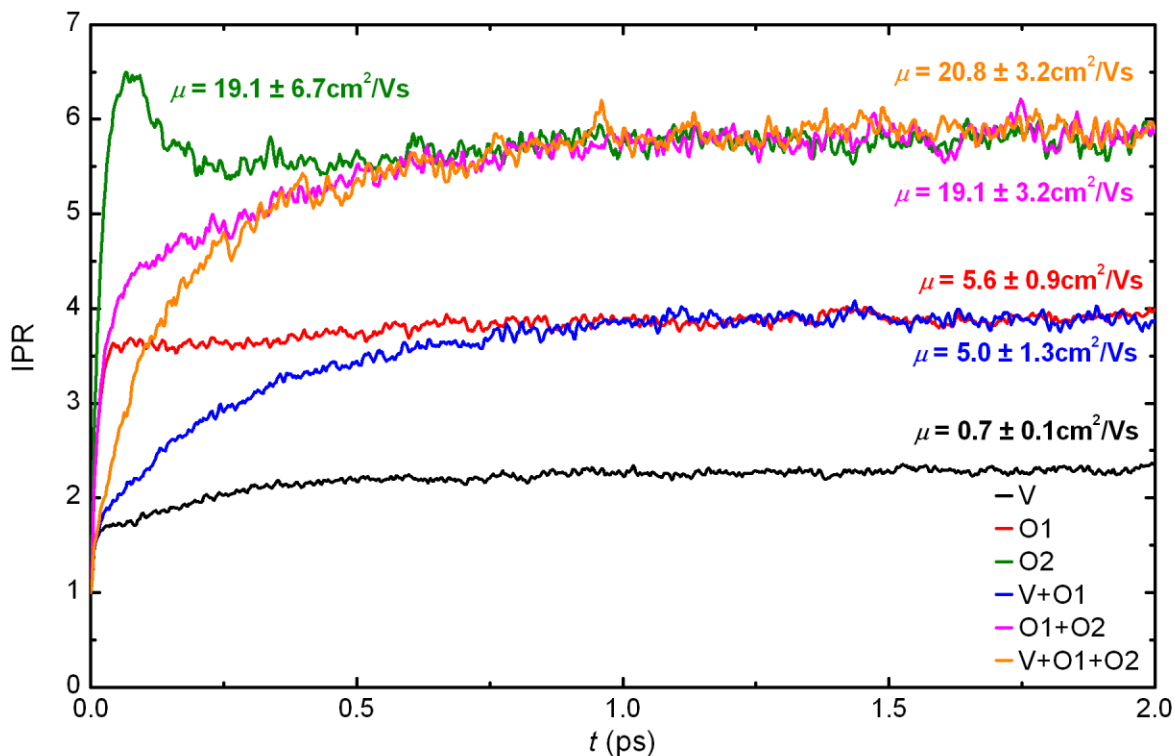# Inverse participation ratio time series for the TMT molecular crystal

Fig. S-14 The time evolution of the IPR values for the TMT molecular crystal for variable QM embedding schemes. Cases "V", "O1", and "O2" correspond to single QM-active wires embedded into the bulk crystal, "V+O1" and "O1+O2" correspond to twin wire configurations, and "V+O1+O2" refers to the case when all translational invariant nanowires are taken into consideration. Room temperature hole mobility for each case is highlighted inside the diagram.

References

D. Andrienko, V. Markon and K. Kremer, *J. Chem. Phys.*, 2006, **125**, 124902.

A.D. Becke, *J. Chem. Phys.*, 1993, **98**, 5648.

A. Carof, S. Giannini and J. Blumberger, J. Chem. Phys., 2017, **147**, 214113.

G. Cinacchi, R. Colle and A. Tani, *J. Phys. Chem. B*, 2004, **108**, 7969.

F. Gajdos, S. Valner, F. Hoffmann, J. Spencer, M. Breuer, A. Kubas, M. Dupuis and J. Blumberger, *J. Chem. Theory Comput.*, 2014, **10**, 4653–4660.

S. Giannini, A. Carof and J. Blumberger, J. Phys. Chem. Lett., 2018, **9**, 3116-3123.

G. Granucci and M. Persico, J. Chem. Phys., 2007, **126**, 134114.

W.L. Jorgensen and D.L. Severance, *J. Am. Chem. Soc.*, 1990, **112**, 4768.

W.L. Jorgensen, J.D. Madura and C.J. Swenson, *J. Am. Chem. Soc.*, 1984, **106**, 6638.

A. Kubas, F. Hoffmann, A. Heck, H. Oberhofer, M. Elstner and J. Blumberger, *J. Chem. Phys.*, 2014, **140**, 104105.

C. Lee, W. Yang and R. G. Parr, *Phys. Rev. B*, 1988, **37**, 785.

V. Marcon, T. Vehoff, J. Kirkpatrick, C. Jeong, D.Y. Yoon, K. Kremer and D. Andrienko, *J. Chem. Phys.*, 2008, **129**, 094505.

G.J. Martyna, D.J. Tobias and M.L. Klein, *J. Chem. Phys.*, 1994, **101**, 4177.

J. P. Perdew, K. Burke and M. Ernzerhof, *Phys. Rev. Lett.*, 1996, **77**, 3865.

J. P. Perdew and M. Ernzerhof , *J. Chem. Phys.*, 1996, **105**, 9982.

J. Spencer, F. Gajdos and J. Blumberger, J. Chem. Phys., 2016, **145**, 064102.

J. C. Tully, J. Chem. Phys., 1990, **93**, 1061-1071.

N. Troullier and J. L. Martins, *Phys. Rev. B*, 1991, **43**, 1993.

L. Wang and O. V. Prezhdo, J. Phys. Chem. Lett., 2014, **5**, 713.

J. Wang, R.M. Wolf, J.W. Caldwell, P.A. Kollman and D.A. Case*, J. Comput. Chem.*, 2004, **25**, 1157.

O. G. Ziogos, S. Konstantinopoulos, L. Tsetseris and D. N. Theodorou, *J. Phys. Chem. C*, 2018, **122**, 18715-18731.

O. G. Ziogos and D. N. Theodorou, *Mol. Phys.*, 2015, **113**, 2776-2790.